On the Origin of Abundance Variations in the Milky Way's High-α Plateau

Tawny Sit[1] , David H. Weinberg[1] , and Emily J. Griffith[2,3]

[1] Department of Astronomy and Center of Cosmology and AstroParticle Physics, The Ohio State University, Columbus, OH 43210, USA; sit.6@osu.edu
[2] Center for Astrophysics and Space Astronomy, Department of Astrophysical and Planetary Sciences, University of Colorado, 389 UCB, Boulder, CO 80309-0389, USA

Abstract

Using multielement abundances from the Sloan Digital Sky Survey APOGEE survey, we investigate the origin of abundance variations in Milky Way (MW) disk stars on the "high-α plateau," with $-0.5 \leqslant [\mathrm{Mg/H}] \leqslant -0.1$ and $0.25 \leqslant [\mathrm{Mg/Fe}] \leqslant 0.35$. The elevated $[\alpha/\mathrm{Fe}]$ ratios of these stars imply low enrichment contributions from Type Ia supernovae (SN Ia), but it is unclear whether their abundance patterns reflect pure core-collapse supernova (CCSN) enrichment. We find that plateau stars with higher $[\mathrm{Fe/Mg}]$ ratios also have higher $[\mathrm{X/Mg}]$ ratios for other iron-peak elements, suggesting that the $[\mathrm{Fe/Mg}]$ variations in the plateau population do reflect variations in the SN Ia/CCSN ratio. To quantify this finding, we fit the observed abundance patterns with a two-process model, calibrated on the full MW disk, which represents each star's abundances as the sum of a prompt CCSN process with amplitude A_{cc} and a delayed SN Ia process with amplitude A_{Ia}. This model is generally successful at explaining the observed trends of $[\mathrm{X/Mg}]$ with $A_{\mathrm{Ia}}/A_{\mathrm{cc}}$, which are steeper for elements with a large SN Ia contribution (e.g., Cr, Ni, Mn) and flatter for elements with low SN Ia contribution (e.g., O, Si, Ca). Our analysis does not determine the value of $[\mathrm{Mg/Fe}]$ corresponding to pure CCSN enrichment, but it should be at least as high as the upper edge of the plateau at $[\mathrm{Mg/Fe}] \approx 0.35$, and could be significantly higher. Compared to the two-process predictions, the observed trends of $[\mathrm{X/Mg}]$ with $A_{\mathrm{Ia}}/A_{\mathrm{cc}}$ are steeper for (C+N) but shallower for Ce, providing intriguing but contradictory clues about asymptotic giant branch enrichment in the early disk.

Unified Astronomy Thesaurus concepts: Chemical abundances (224); Chemical enrichment (225); Galaxy chemical evolution (580); Milky Way disk (1050)

1. Introduction

Stars in the Milky Way (MW) disk follow two distinct sequences in the plane of $[\alpha/\mathrm{Fe}]$ versus $[\mathrm{Fe/H}]$, with the "high-α" and "low-α" populations associated (though not perfectly: see M. R. Hayden et al. 2017) with the kinematic hot, thick disk and the cold, thin disk, respectively. Low-α stars are generally younger than high-α stars of the same metallicity, and the lower (around solar) $[\alpha/\mathrm{Fe}]$ is understood as a consequence of greater Fe enrichment from time-delayed Type Ia supernovae (SN Ia) (e.g., F. Matteucci & L. Greggio 1986; A. McWilliam 1997; K. Fuhrmann 1998; T. Bensby et al. 2003; V. Z. Adibekyan et al. 2012). While the "knee" where the $[\alpha/\mathrm{Fe}]$ ratio begins to decrease with increasing metallicity is a signature of SN Ia enrichment in the thick disk (e.g., S. Feltzing et al. 2003), a common assumption is that the $[\alpha/\mathrm{Fe}]$ ratios in the high-α population at metallicities below the knee, where the $[\alpha/\mathrm{Fe}]$ trend is mostly flat, reflect the yield ratios for pure core-collapse supernova (CCSN) enrichment, averaged over the stellar initial mass function (IMF) and other progenitor properties, such as rotation and binarity. Alternatively, the higher $[\alpha/\mathrm{Fe}]$ ratio could represent a mix of SN Ia and CCSN contributions, but with a SN Ia/CCSN ratio lower than that of the low-α population. In either case, it is more physically accurate to describe the "high-α" and "low-α" populations as "low-Ia"

and "high-Ia," respectively, which is the nomenclature we adopt in the rest of this paper. Using data from the Sloan Digital Sky Survey APOGEE survey (S. R. Majewski et al. 2017), S. Bertran de Lis et al. (2016) estimate an intrinsic scatter of ~ 0.04 dex in $[\mathrm{O/Fe}]$ at fixed $[\mathrm{Fe/H}]$ *within* the low-Ia population. Similarly, F. Vincenzo et al. (2021) estimate intrinsic scatter of $\sim 0.03\text{–}0.04$ dex in the low-Ia population for $[\mathrm{O/Fe}]$, $[\mathrm{Mg/Fe}]$, $[\mathrm{Si/Fe}]$, and $[\mathrm{Ca/Fe}]$.

In this paper, we investigate the abundance scatter of 17 elements within the low-Ia population. A key question is whether abundance scatter within the low-Ia population is driven primarily by variations in the SN Ia/CCSN ratio or arises instead from other effects, such as stochastic sampling of the supernova population. If there are significant variations of SN Ia/CCSN within the low-Ia population, then elements that have a large SN Ia contribution should vary together. For example, stars that are high in $[\mathrm{Fe/Mg}]$ should also be high in $[\mathrm{Ni/Mg}]$ and $[\mathrm{Mn/Mg}]$, where we have adopted Mg as our reference element because it is expected to arise entirely from CCSN with little metallicity dependence (see, e.g., K. Nomoto et al. 2013; B. H. Andrews et al. 2017, and references therein). Conversely, elements whose production is dominated by CCSN should exhibit low scatter in $[\mathrm{X/Mg}]$ at fixed $[\mathrm{Mg/H}]$.

To implement this idea quantitatively, we adopt the two-process model (E. Griffith et al. 2019; D. H. Weinberg et al. 2019, 2022; E. J. Griffith et al. 2022, 2024 hereafter G24; T. Sit et al. 2024), which describes a star's multielement abundances as the sum of enrichment from a prompt process associated with CCSN and a delayed process associated with SN Ia. The two-process model has been successful at predicting the multielement abundance pattern of stars in the MW disk to $\approx 0.02\text{–}0.05$ dex accuracy, comparable to the

---

observational uncertainties reported by large spectroscopic surveys. At each [Mg/H], the relative contribution of the two processes for a given element X is inferred from the gap in median [X/Mg] between the disk's low-Ia and high-Ia populations. If abundance scatter in the low-Ia population comes mainly from SN Ia/CCSN variation, then the two-process model should predict the element-by-element trends within this population, even though it is calibrated to the difference between low-Ia and high-Ia stars. However, the two-process model is limited by its namesake two processes, SN Ia and CCSN, so deviations can be indicative of other nucleosynthetic pathways, such as enrichment from asymptotic giant branch (AGB) stars (E. J. Griffith et al. 2022; D. H. Weinberg et al. 2022). Therefore, we can also investigate the contribution of any additional processes to the abundance scatter in the low-Ia plateau.

We concentrate our analysis on low-Ia stars with $-0.5 \leqslant [\text{Mg/H}] \leqslant -0.1$, a range where the median trend of [Mg/Fe] with [Mg/H] is well described by a flat "plateau" at $[\text{Mg/Fe}]_{\text{pl}} \approx 0.3$. Many observational studies show this plateau continuing down to [Fe/H] ≈ -2.5, with similar flat plateaus for [Si/Fe] and [Ca/Fe] (see, e.g., C. Kobayashi et al. 2020a). It is tempting, therefore, to identify these plateau ratios with the ratios produced by CCSN alone. However, the star-to-star scatter and study-to-study variations become larger at [Fe/H] < −1. Furthermore, C. Conroy et al. (2022) find that in situ halo stars show a trend of declining [Mg/Fe] with increasing [Fe/H] for [Fe/H] < −1.5, rather than a flat plateau. They propose a model in which the true ratio from CCSN enrichment corresponds to $[\text{Mg/Fe}]_{\text{cc}} \approx 0.6$, and the roughly flat trend of [Mg/Fe] in the thick disk reflects a balance between SN Ia and CCSN enrichment during an epoch of accelerating star formation (see also D. Maoz & O. Graur 2017; B. Chen et al. 2023).

The two-process model recasts each star's abundances into two amplitude parameters corresponding to the level of prompt (CCSN) and delayed (SN Ia) contribution, and the element-by-element residuals between the observed abundances and the model predictions. Both the "process vectors" describing the relative element contributions and the inferred values of the star-by-star "process amplitudes" depend on the value of [Mg/Fe] that is assumed to represent pure-CCSN enrichment (see Section 3 below). We originally hoped that our analysis could distinguish a scenario in which the low-Ia plateau reflects CCSN only from a scenario in which SN Ia enrichment is already substantial at [Mg/Fe] ≈ 0.3. However, we show in Section 3.1 that the residual abundances from the two-process predictions are independent of the assumed $[\text{Mg/Fe}]_{\text{cc}}$, even though the process amplitudes are not (see also G24). Unfortunately, this means that our results do not shed light on the true level of $[\text{Mg/Fe}]_{\text{cc}}$, though they do provide strong evidence for variation of the SN Ia/CCSN ratio within the low-Ia population.

This paper is organized as follows. Section 2 introduces the abundance data we use. In Section 3, we discuss the two-process model in detail, showing that it predicts abundances through a simple linear interpolation of median *linear* abundance ratios and that the predicted abundances are independent of the assumed $[\text{Mg/Fe}]_{\text{cc}}$ as a result. Section 4 examines the sources of observed scatter around the median [X/Mg] values in the low-Ia plateau, where we find that variation in SN Ia/CCSN contributes strongly to the observed

intrinsic dispersion. In Section 5, we summarize our results and discuss future avenues for studying the information encoded in the intrinsic dispersion patterns of abundances in the Galaxy.

2. Data

Systematic trends in abundance measurements with $\log(g)$ and T_{eff} can cause changes in median abundance trends (E. Griffith et al. 2021) or, more importantly for this study, add correlated scatter between elements (D. H. Weinberg et al. 2022). These trends are most likely an artifact of the spectral fitting process, since a star's $\log(g)$ changes during its post-main sequence lifetime, but the abundances of most elements should stay the same. T. Sit et al. (2024, hereafter S24) present corrected abundances for 288,789 stars from APOGEE DR17 (Abdurro'uf et al. 2022), where artificial trends in APOGEE abundances with stellar surface gravity $\log(g)$ were identified and removed. This $\log(g)$ calibration also removes trends with stellar effective temperature T_{eff}.

In this work, we use a calibration sample and a smaller plateau sample, both selected from the full S24 catalog. Our calibration sample is the same as that of S24, whose selection criteria are:

1. $-0.75 \leqslant [\text{Mg/H}] \leqslant 0.45$
2. $\log(g) = 0 - 3.5$
3. $T_{\text{eff}} = 3000-5500$ K
4. $R = 3-15$ kpc
5. $|Z| < 2$ kpc
6. `EXTRATARG==0`
7. SNR $\geqslant 100$

The calibration sample consists of 149,904 stars from APOGEE DR17.

We also generate a smaller plateau sample of stars that occupy a well-populated region on the low-Ia plateau and is a subset of the calibration sample. We apply the following cuts in [Fe/Mg] and [Mg/H] to the calibration sample to define the plateau sample:

1. $-0.5 \leqslant [\text{Mg/H}] \leqslant -0.1$
2. $-0.35 \leqslant [\text{Fe/Mg}] \leqslant -0.25$

These cuts select the region with the highest density of plateau stars around the $[\text{Mg/Fe}]_{\text{cc}} = 0.3$ value used in D. H. Weinberg et al. (2022) and S24. The plateau sample contains 10,262 stars.

Figure 1 shows the calibration sample, divided into low-Ia and high-Ia populations, and the additional [Mg/Fe] and [Fe/H] cuts that define the plateau sample. The low-Ia population is defined as

$$\begin{cases} [\text{Mg/Fe}] > 0.12 - 0.13[\text{Fe/H}], & [\text{Fe/H}] < 0 \\ [\text{Mg/Fe}] > 0.12, & [\text{Fe/H}] > 0. \end{cases} \quad (1)$$

For this division between the low-Ia and high-Ia populations only, we use the raw ASPCAP values (i.e., prior to the $\log(g)$ calibration). This maintains consistency with S24 in the median [X/Mg] sequences of each population from which the "process vectors" of the two-process model are derived (see Section 3), so that we better isolate the effect of varying the assumed core-collapse [Fe/Mg] ratio in the two-process model in Section 3. After accounting for flat offsets applied during calibration (see S24 for details), applying the $\log(g)$
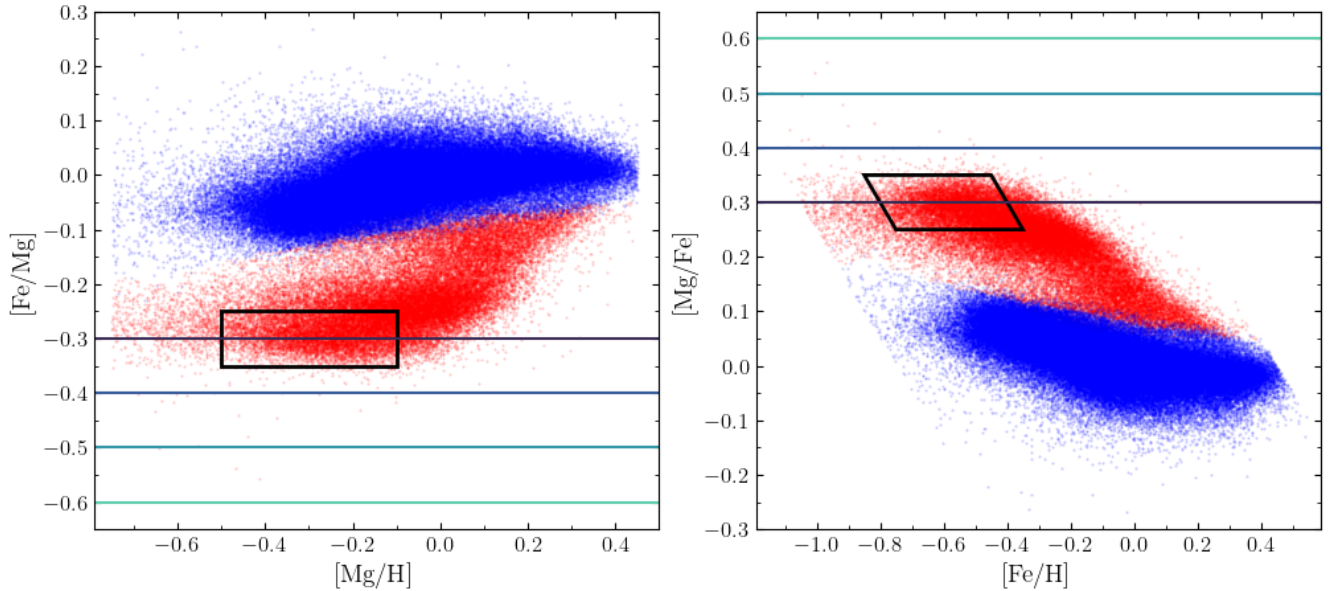
Figure 1. Low-Ia (red) and high-Ia (blue) APOGEE DR17 stars from the calibration sample of the S24 catalog in [Fe/Mg]–[Mg/H] space (left) and [Mg/Fe]–[Fe/H] space (right). Plotted abundances are the S24 log(g)-calibrated abundances. The sample selection criteria (see Section 2) for low-Ia plateau stars ("plateau sample") analyzed in this work are indicated by the black lines. The four different [Fe/Mg]$_{cc}$ assumptions ([Fe/Mg]$_{cc}$ = −0.3, −0.4, −0.5, −0.6) tested in Section 3 are indicated by the horizontal lines.

calibrations would change the high/low-Ia classification of only 1% of the calibration sample, and only for stars near the division boundary (none of which are in the plateau sample).

We utilize 17 elements, also analyzed by S24, spanning a range of nucleosynthetic sources: O, Si, S, and Ca (α elements); C+N, Na, Al, and K (light odd-Z elements); Cr, Fe, Ni, V, Mn, Co, and Cu (iron-peak elements); and Ce (s-process element). The combined element C+N accounts for the surface abundances of C and N changing as a star evolves up the red giant branch while the total number of nuclei remains nearly equal to the birth abundance. S24 incorporated abundance measurements from the BAWLAS catalog (C. R. Hayes et al. 2022) into their analysis for O, C+N, S, Na, V, and Ce, but we use the ASPCAP measurements for this work to increase the sample size of available measurements, since BAWLAS used a higher signal-to-noise ratio (SNR) threshold of SNR ⩾ 150. Cu is on the sharply falling edge of the iron peak ("Fe-cliff") and though its astrophysical origins are debated, literature suggests more significant contributions from massive stars (e.g., S. E. Woosley & T. A. Weaver 1995; D. Romano & F. Matteucci 2007; C. Kobayashi et al. 2020a), so it may have different nucleosynthesis patterns from the other Fe-peak elements. Therefore, despite being measured only by BAWLAS, we proceed with including Cu in this study, but note that only 2277 out of 10,262 stars in our sample have a Cu measurement.

As part of our analysis in this paper, we use the reported measurement errors from ASPCAP (or BAWLAS, for Cu). The measurement uncertainties in DR17 are based on the process for DR16, where a function of $T_{\rm eff}$, [M/H], and SNR is fitted to the deviations in measured abundances from repeat observations (see Section 5.4 of H. Jönsson et al. 2020 for more details). A similar procedure using repeat measurements is used for the empirical BAWLAS uncertainties (see Section 4.7.2 in C. R. Hayes et al. 2022) we use for Cu.

3. The Two-process Model

The two-process model is a semiempirical nucleosynthesis model that describes a star's multielement abundances as a sum of two contributions, associated with CCSN and SN Ia, with amplitudes $A_{\rm cc}$ and $A_{\rm Ia}$. The processes are anchored in observed median [X/Mg] trends with metallicity, which have been observed to be nearly independent of location across the Galactic disk provided the low-Ia and high-Ia populations are separated (D. H. Weinberg et al. 2019). By interpreting these spatially invariant trends as driven by nucleosynthetic yields rather than spatially varying quantities such as the star formation history, the relative contribution to different elements is taken to be universal for each process (though it may depend on metallicity). These relative contributions reflect the population-averaged yields of CCSN and SN Ia, where the population-average includes averages over the stellar IMF, binary properties, rotation, and other parameters that affect yields. In the notation of D. H. Weinberg et al. (2022, hereafter W22), the abundances predicted by the two-process model are

$$[{\rm X/H}]_{\rm 2proc} = \log_{10}(A_{\rm cc}q_{\rm cc}^{\rm X} + A_{\rm Ia}q_{\rm Ia}^{\rm X}), \qquad (2)$$

where the "process vectors" $q_{\rm cc}^{\rm X}$ and $q_{\rm Ia}^{\rm X}$ are derived from the ensemble of stars and the amplitudes $A_{\rm cc}$ and $A_{\rm Ia}$ are fitted to each star individually.

The two-process model can successfully predict stellar abundances in the MW disk to 0.02–0.05 dex on average (e.g., E. Griffith et al. 2019; D. H. Weinberg et al. 2019; W22), and similar accuracy has been achieved with other two-parameter models conditioned on age and [Fe/H] (M. K. Ness et al. 2019) or α and Fe abundances (M. K. Ness et al. 2022; B. L. Ratcliffe & M. K. Ness 2023). However, a star's actual abundances may differ from the two-process prediction because additional processes contribute or because the CCSN and SN Ia processes are not completely universal. The
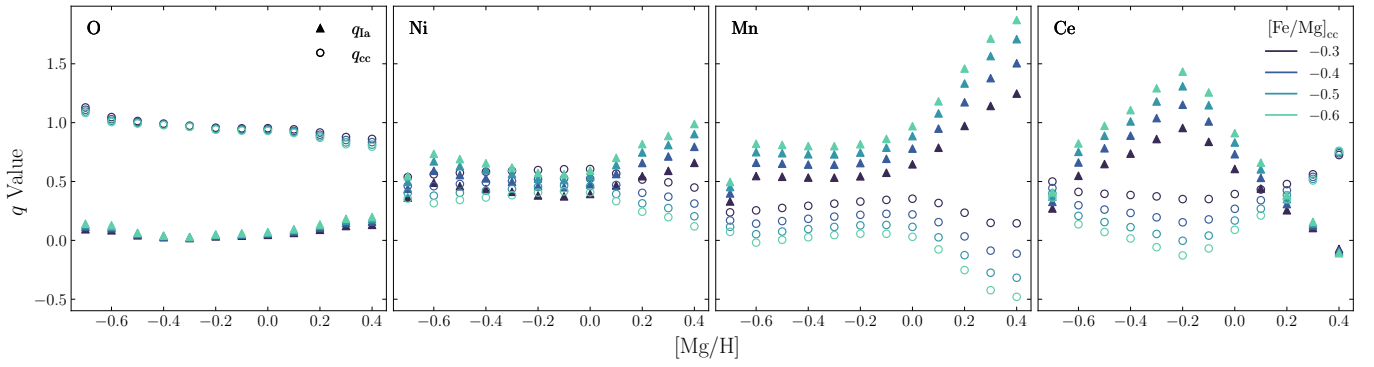
Figure 2. $q_{\mathrm{Ia}}^{\mathrm{X}}$ (filled triangles) and $q_{\mathrm{cc}}^{\mathrm{X}}$ (open circles) vectors as a function of metallicity for X = O, Ni, Mn, and Ce, derived from the full S24 calibration sample. Colors indicate different assumed plateau values, with increasingly light colors reflecting a decreasing $[\mathrm{Fe/Mg}]_{\mathrm{cc}}$ value (or increasing $[\mathrm{Mg/Fe}]_{\mathrm{pl}}$); the colors match the lines depicted in Figure 1.

approach can be generalized to include additional processes (W22; G24), though these become more difficult to disentangle as the number of processes increases. More generally, one can think of the two processes as representing prompt and time-delayed nucleosynthesis contributions, and the two-process model is reasonably successful at predicting abundances of elements whose delayed contribution is expected to arise from AGB stars rather than SN Ia, such as C, N, Ce, Y, and Ba (E. J. Griffith et al. 2022; W22).

3.1. Process Vectors and Amplitudes

Without loss of information, one can express a star's measured abundances in terms of the two-process amplitudes A_{cc} and A_{Ia}, which characterize the overall level of prompt and delayed enrichment, and residuals from the two-process prediction

$$\Delta[\mathrm{X/H}]_{2\mathrm{proc}} = [\mathrm{X/H}]_{\mathrm{meas}} - [\mathrm{X/H}]_{2\mathrm{proc}}. \quad (3)$$

For present purposes, we would like to know how the predicted and residual abundances depend on the value $[\mathrm{Fe/Mg}]_{\mathrm{cc}}$ that is assumed to represent the iron-to-magnesium ratio from CCSN enrichment with no SN Ia contribution. We test assumptions of $[\mathrm{Fe/Mg}]_{\mathrm{cc}}$ values spaced at 0.1 dex intervals between $[\mathrm{Fe/Mg}]_{\mathrm{cc}} = -0.3$, the fiducial assumption from W22 and S24, and $[\mathrm{Fe/Mg}]_{\mathrm{cc}} = -0.6$, approximately the value estimated by C. Conroy et al. (2022). We follow the definition and equations of W22, and to simplify expressions we introduce the notation

$$\{\mathrm{X/Y}\} = 10^{[\mathrm{X/Y}]}, \quad (4)$$

i.e., $\{\mathrm{X/Y}\}$ is simply the linear abundance ratio of elements X and Y scaled by the solar ratio. W22 derive the two-process vectors from the median abundance ratio of stars in the low-Ia and high-Ia disk populations, $[\mathrm{X/Mg}]_{\mathrm{low}}$ and $[\mathrm{X/Mg}]_{\mathrm{high}}$, respectively, in bins of $[\mathrm{Mg/H}]$.[4] They assume that Mg comes entirely from CCSN and use $\{\mathrm{Fe/Mg}\}$ as an indicator of the amount of SN Ia enrichment.

One can use Equations (21)–(26) of W22 to show that

$$q_{\mathrm{cc}}^{\mathrm{X}} = \{\mathrm{X/Mg}\}_{\mathrm{low}} - (\{\mathrm{X/Mg}\}_{\mathrm{high}} - \{\mathrm{X/Mg}\}_{\mathrm{low}})$$

$$\times \left(\frac{\{\mathrm{Fe / Mg}\}_{\mathrm{low}} - \{\mathrm{Fe / Mg}\}_{\mathrm{cc}}}{\{\mathrm{Fe / Mg}\}_{\mathrm{high}} - \{\mathrm{Fe / Mg}\}_{\mathrm{low}}} \right) \quad (5)$$

and

$$q_{\mathrm{Ia}}^{\mathrm{X}} = (\{\mathrm{X/Mg}\}_{\mathrm{high}} - \{\mathrm{X/Mg}\}_{\mathrm{low}})$$

$$\times \left(\frac{1 - \{\mathrm{Fe / Mg}\}_{\mathrm{cc}}}{\{\mathrm{Fe / Mg}\}_{\mathrm{high}} - \{\mathrm{Fe / Mg}\}_{\mathrm{low}}} \right). \quad (6)$$

Expressed in these linear, solar-scaled ratios, the value of $q_{\mathrm{Ia}}^{\mathrm{X}}$ follows from the gap in $\{\mathrm{X/Mg}\}$ between the high-Ia and low-Ia populations, divided by the gap in $\{\mathrm{Fe/Mg}\}$ between these populations relative to the total gap between the CCSN ratio and the solar ratio. If $\{\mathrm{X/Mg}\}$ is the same for low-Ia and high-Ia stars, then $q_{\mathrm{Ia}}^{\mathrm{X}} = 0$, and $q_{\mathrm{cc}}^{\mathrm{X}}$ is simply the solar-scaled $\{\mathrm{X/Mg}\}$. Equations (5) and (6) are applied in each $[\mathrm{Mg/H}]$ bin. The assumed value of $\{\mathrm{Fe/Mg}\}_{\mathrm{cc}}$ can in principle change with $[\mathrm{Mg/H}]$, though W22 adopt a single value based on the plateau in $[\mathrm{Mg/Fe}]$ observed for low-metallicity, low-Ia disk stars, while G24 include a possible tilt in this plateau.

Figure 2 plots $q_{\mathrm{Ia}}^{\mathrm{X}}$ and $q_{\mathrm{cc}}^{\mathrm{X}}$ as a function of $[\mathrm{Mg/H}]$ with different $[\mathrm{Fe/Mg}]_{\mathrm{cc}}$ assumptions for four illustrative elements. $q_{\mathrm{Ia}}^{\mathrm{X}}$ and $q_{\mathrm{cc}}^{\mathrm{X}}$ are derived from the calibration sample described in Section 2. Keeping in mind that the two-process model, as defined by W22, fixes $q_{\mathrm{Ia}}^{\mathrm{Mg}} = 0$ and $q_{\mathrm{cc}}^{\mathrm{Mg}} = 1$ irrespective of the assumed plateau value, we observe that changing the $[\mathrm{Fe/Mg}]_{\mathrm{cc}}$ assumption does not significantly change $q_{\mathrm{Ia}}^{\mathrm{O}}$ and $q_{\mathrm{cc}}^{\mathrm{O}}$ because O is an α element like Mg. The other elements illustrated here (Ni, Mn, and Ce) all have a significant delayed contribution from SN Ia (Ni and Mn) or AGB stars (Ce). For these elements, $q_{\mathrm{Ia}}^{\mathrm{X}}$ increases with decreasing $[\mathrm{Fe/Mg}]_{\mathrm{cc}}$, while $q_{\mathrm{cc}}^{\mathrm{X}}$ decreases; however, the overall shape of the metallicity-dependent q-vector stays the same. The gap between the $[\mathrm{Fe/Mg}]_{\mathrm{cc}} = -0.5$ and $[\mathrm{Fe/Mg}]_{\mathrm{cc}} = -0.6$ sequences is also smaller than the gap between $[\mathrm{Fe/Mg}]_{\mathrm{cc}} = -0.3$ and $[\mathrm{Fe/Mg}]_{\mathrm{cc}} = -0.4$ or $[\mathrm{Fe/Mg}]_{\mathrm{cc}} = -0.4$ and $[\mathrm{Fe/Mg}]_{\mathrm{cc}} = -0.5$.

For individual stars, the amplitudes A_{cc} and A_{Ia} can be inferred from the star's $[\mathrm{Mg/H}]$ and $[\mathrm{Fe/Mg}]$ alone using Equations (13) and (18) of W22 (e.g., D. H. Weinberg et al. 2019; S. Hasselquist et al. 2024). In terms of linear ratios, these equations can be written as

$$A_{\mathrm{cc}} = \{\mathrm{Mg/H}\} \quad (7)$$

and

$$A_{\mathrm{Ia}} = A_{\mathrm{cc}} \times \left(\frac{\{\mathrm{Fe/Mg}\} - \{\mathrm{Fe/Mg}\}_{\mathrm{cc}}}{1 - \{\mathrm{Fe/Mg}\}_{\mathrm{cc}}} \right). \quad (8)$$

---

[4] G24 present an alternative method that derives $q_{\mathrm{cc}}^{\mathrm{X}}$ and $q_{\mathrm{Ia}}^{\mathrm{X}}$ from global fits to the ensemble of stellar abundances; the two approaches give very similar results.
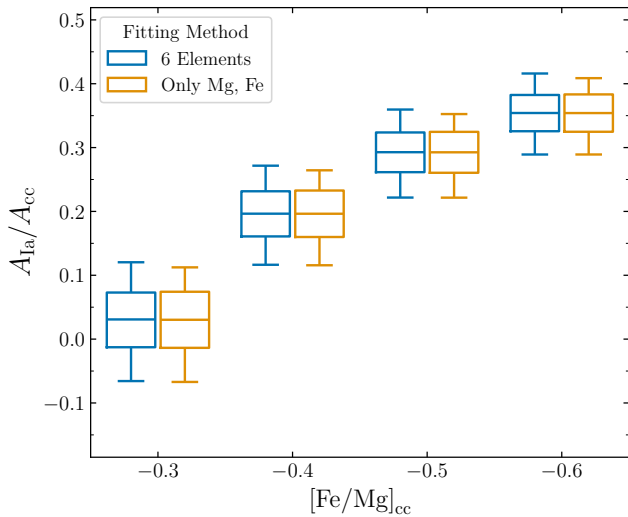
Figure 3. Box-and-whisker plot showing the distribution of the inferred ratio of SN Ia to CCSN contribution, $A_{\mathrm{Ia}}/A_{\mathrm{cc}}$, using the two-process model for different assumed $[\mathrm{Mg}/\mathrm{Fe}]_{\mathrm{cc}}$, for the plateau sample defined in Section 2. The center horizontal line indicates the median, boxes indicate the interquartile (25th–75th percentile) range, and tails indicate the 5th–95th percentile range of the data. A_{cc} and A_{Ia} are inferred using Equations (7) and (8) for the orange boxes. A_{cc} and A_{Ia} are calculated using a χ^2-minimization procedure to the six elements Mg, O, Si, Ca, Fe, and Ni as described in W22 and S24 for the blue boxes.

Thus, in this case, the ratio $A_{\mathrm{Ia}}/A_{\mathrm{cc}}$ is simply a linear transformation of the linear $\{\mathrm{Fe}/\mathrm{Mg}\}$ ratio.

Instead of using only $[\mathrm{Mg}/\mathrm{H}]$ and $[\mathrm{Fe}/\mathrm{Mg}]$, A_{cc} and A_{Ia} can also be estimated from a fit to multiple abundances (e.g., W22; G24; S24). Using multiple elements reduces the effects of random measurement errors in Mg and Fe that may induce artificial correlations in the residual abundances (Y.-S. Ting & D. H. Weinberg 2022; W22). More specifically, in this work, we adopt the fitting procedure used in W22 and S24—χ^2 minimization to six well-measured APOGEE elements with a range of relative CCSN and SN Ia contributions: O, Mg, Si, Ca, Fe, and Ni.

For stars in the plateau sample (see Section 2), we use S24 $\log(g)$-calibrated abundances to derive A_{cc} and A_{Ia}. Figure 3 shows how the distribution of $A_{\mathrm{Ia}}/A_{\mathrm{cc}}$ values shifts to higher values as lower $\{\mathrm{Fe}/\mathrm{Mg}\}_{\mathrm{cc}}$ values are assumed. The overall $A_{\mathrm{Ia}}/A_{\mathrm{cc}}$ distribution at fixed $[\mathrm{Fe}/\mathrm{Mg}]_{\mathrm{cc}}$ is very similar between the Fe and Mg calculation (using Equations (7)–(8)) and the six-element fit; the main notable difference is a slightly longer tail toward high $A_{\mathrm{Ia}}/A_{\mathrm{cc}}$ for the six-element fit. The shift from $[\mathrm{Fe}/\mathrm{Mg}]_{\mathrm{cc}} = -0.5$ and $[\mathrm{Fe}/\mathrm{Mg}]_{\mathrm{cc}} = -0.6$ is smaller than $[\mathrm{Fe}/\mathrm{Mg}]_{\mathrm{cc}} = -0.3$ to $[\mathrm{Fe}/\mathrm{Mg}]_{\mathrm{cc}} = -0.4$, similarly to how the $q_{\mathrm{Ia}}^{\mathrm{X}}$ and $q_{\mathrm{cc}}^{\mathrm{X}}$ sequences shift in Figure 2 for Ni, Mn, and Ce. Additionally, there are no variations in $A_{\mathrm{Ia}}/A_{\mathrm{cc}}$ correlated with guiding radius R_{guide} or maximum height from the midplane Z_{max} within the plateau sample. These values are taken from the astroNN catalog for DR17,[5] which uses Gaia eDR3 for distances via H. W. Leung & J. Bovy (2019) and derives orbital parameters via J. T. Mackereth & J. Bovy (2018).

At $[\mathrm{Fe}/\mathrm{Mg}]_{\mathrm{cc}} = -0.4$, the values of A_{cc} and A_{Ia} are positive over the metallicity and α element range of the plateau sample. This is consistent with G24 and the physical interpretation that

a star cannot have negative contribution from a process. Therefore, in the rest of this paper, all two-process quantities calculated for the plateau sample assume $[\mathrm{Fe}/\mathrm{Mg}]_{\mathrm{cc}} = -0.4$. We will show in Section 3.2 that the choice of $[\mathrm{Fe}/\mathrm{Mg}]_{\mathrm{cc}}$ does not impact the residual abundances (Equation (3)).

Figure 4 shows the distribution of statistical uncertainties in A_{Ia}, A_{cc}, and the ratio $A_{\mathrm{Ia}}/A_{\mathrm{cc}}$ for the six-element fitting method and the Mg–Fe only method, assuming $[\mathrm{Fe}/\mathrm{Mg}]_{\mathrm{cc}} = -0.4$. For each star, $\sigma(A_{\mathrm{Ia}})$ and $\sigma(A_{\mathrm{cc}})$ were calculated by resampling the predicted O, Mg, Si, Ca, Fe, and Ni abundances assuming Gaussian reported star-by-star measurement uncertainties, recalculating A_{Ia} and A_{cc} (using both methods) for each sample, and then calculating the standard deviation of the new A_{Ia} and A_{cc} values over all samples. The distance between the $\sigma(A_{\mathrm{Ia}})$ and $\sigma(A_{\mathrm{cc}})$ histogram peaks in Figure 4 shows that using the six-element fit slightly reduces the uncertainty in the A_{Ia} and A_{cc} values due to measurement uncertainties, by 0.005–0.01.

3.2. Residual Abundances and Linearity

From Equations (5)–(8), it is straightforward to show that the abundances predicted by the two-process model are

$$\{\mathrm{X}/\mathrm{Mg}\}_{\mathrm{pred}} = \{\mathrm{X}/\mathrm{Mg}\}_{\mathrm{low}} + (\{\mathrm{Fe}/\mathrm{Mg}\} - \{\mathrm{Fe}/\mathrm{Mg}\}_{\mathrm{low}})$$
$$\times \left(\frac{\{\mathrm{X}/\mathrm{Mg}\}_{\mathrm{high}} - \{\mathrm{X}/\mathrm{Mg}\}_{\mathrm{low}}}{\{\mathrm{Fe}/\mathrm{Mg}\}_{\mathrm{high}} - \{\mathrm{Fe}/\mathrm{Mg}\}_{\mathrm{low}}} \right).$$

$$(9)$$

When $q_{\mathrm{cc}}^{\mathrm{X}}$ and $q_{\mathrm{Ia}}^{\mathrm{X}}$ are inferred from median abundance trends of low-Ia and high-Ia stars, and A_{cc} and A_{Ia} are inferred from $[\mathrm{Mg}/\mathrm{H}]$ and $[\mathrm{Fe}/\mathrm{Mg}]$, the predicted $\{\mathrm{X}/\mathrm{Mg}\}$ ratios are simply a linear interpolation (or extrapolation) of the median $\{\mathrm{X}/\mathrm{Mg}\}$ ratios in the low-Ia and high-Ia populations, with $\{\mathrm{Fe}/\mathrm{Mg}\}$ as the interpolation variable. This mathematically simple result is not obvious from the W22 equations because they are expressed in logarithmic abundance ratios $[\mathrm{X}/\mathrm{Mg}]$ and $[\mathrm{Fe}/\mathrm{Mg}]$. Figure 5 illustrates the linear behavior for two example elements, Si (an α element with primarily CCSN enrichment) and Mn (a Fe-peak element with very significant SN Ia enrichment). In this figure, solid lines connect the high- and low-Ia median points of the calibration sample at fixed $[\mathrm{Mg}/\mathrm{H}]$ and *are* the predicted linear abundance ratios $\{\mathrm{X}/\mathrm{Mg}\}$ at that $[\mathrm{Mg}/\mathrm{H}]$. The slope of the line represents the extent to which variation in $\{\mathrm{X}/\mathrm{Mg}\}$ is predicted to vary with $\{\mathrm{Fe}/\mathrm{Mg}\}$; it is shallower for a CCSN element such as Si but steeper for a SN Ia element such as Mn in general (though the exact slope and intercept values can change as a function of $[\mathrm{Mg}/\mathrm{H}]$).

Most importantly for our purpose, Equation (9) shows that the predicted abundances, and thus the residual abundances (Equation (3)) are independent of the assumed value of $\{\mathrm{Fe}/\mathrm{Mg}\}_{\mathrm{cc}}$. This result was previously noted by G24, who describe it as an "affine degeneracy" of the two-process model. For different assumed values of $\{\mathrm{Fe}/\mathrm{Mg}\}_{\mathrm{cc}}$, the resulting changes in the process vectors and process amplitudes cancel out exactly so that the predicted abundances remain the same when A_{cc} and A_{Ia} are calculated from only $[\mathrm{Mg}/\mathrm{H}]$ and $[\mathrm{Fe}/\mathrm{Mg}]$.

We reduce the uncertainty in A_{cc} and A_{Ia} from measurement uncertainties by using the six-element χ^2-minimization procedure, so the arguments given above are no longer exact. However, the star-by-star changes in A_{cc}, A_{Ia}, and residual
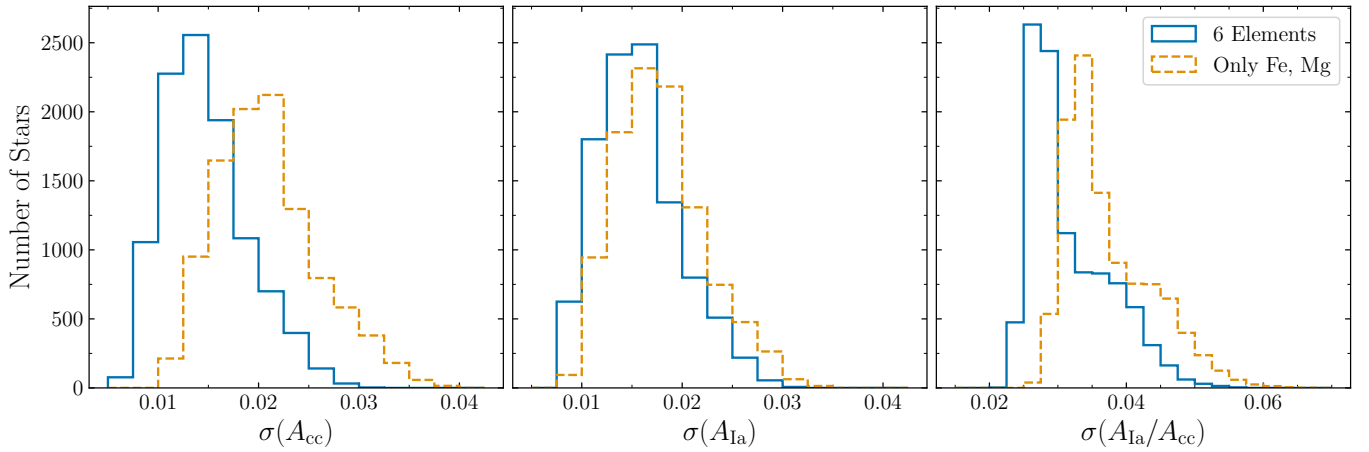
Figure 4. Uncertainty in A_{cc}, $\sigma(A_{cc})$ (left); uncertainty in A_{Ia}, $\sigma(A_{Ia})$ (middle); and uncertainty in A_{Ia}/A_{cc}, $\sigma(A_{Ia}/A_{cc})$ (right) for stars in the plateau sample. For each star, we resample the abundances by drawing from a Gaussian distribution centered at the two-process predicted abundances from the multielement fit with width corresponding to the observational uncertainty. For each sample, we recalculate A_{Ia} and A_{cc}; blue solid lines indicate that A_{Ia} and A_{cc} were inferred from the six-element χ^2-minimization procedure, while orange dashed lines indicate that A_{Ia} and A_{cc} were calculated from only [Mg/H] and [Fe/Mg] using Equations (7) and (8). The uncertainty σ in A_{Ia} and A_{cc} is the standard deviation of the recalculated A_{Ia} and A_{cc} over 500 samples. Values were calculated assuming a plateau value of $[Fe/Mg]_{cc} = -0.4$.

abundances between a two-element and six-element fit are small. By repeating our full procedure with different $[Fe/Mg]_{cc}$ choices, we find that residual abundances are still nearly independent of the adopted value. Therefore, the residual abundances (though not the two-process parameters) presented in the S24 catalog remain valid over all assumptions of $[Fe/Mg]_{cc}$.

4. Abundance Variation in the Low-Ia Plateau

Figure 6 plots [X/Mg] as a function of [Mg/H] for the plateau sample for all elements considered in this work. The overall trend with [Mg/H] is fairly flat for all these elements, but there is significant scatter (except Fe, due to the sample selection criteria). Some of the observed scatter is due to observational uncertainties, whose contribution to the total scatter can be estimated from representative error bars in each panel. Assuming the reported star-by-star measurement uncertainties are correct, the remaining scatter is intrinsic. We wish to understand the origins of this intrinsic scatter, focusing in particular on variation in the SN Ia/CCSN ratio.

The elements Na, Cr, V, Co, and Ce exhibited asymmetric tails of the scatter with [X/Mg] for some stars below the median. We found that the majority of stars contributing to this downward scatter reported ASPCAP [X/H] abundance measurements falling below an upper limit given that star's T_{eff} (for Na, V, and Ce) using the upper limit relations presented in C. R. Hayes et al. (2022), or T_{eff} and SNR (for Cr and Co) from the relations of M. Shetrone et al. (2025, in preparation). The ASPCAP pipeline does not flag upper limits or undetectable abundances. Details on our upper limit flagging procedure and figures showing the affected measurements are presented in Appendix A. The flagged measurements are treated as unreliable and have been removed from all analyses in this section. Furthermore, we found one extreme outlier star with [Cu/Mg] = 1.06, which is most likely a spurious measurement because examination of the spectrum did not show significant absorption in the known Cu line regions. Therefore, this Cu measurement has also been removed from all subsequent analyses.

4.1. Variations Correlated with SN Ia/CCSN Ratio

A plausible source of intrinsic abundance scatter in stars on the low-Ia plateau is the remaining variation in the amount of SN Ia to CCSN contribution. If this effect is dominant, we would expect that elements with significant SN Ia contribution, such as the Fe-peak elements, should vary together, while elements with mostly CCSN contribution, such as the α elements, should exhibit little correlated variation.

We separate the scatter from overall trends by defining the quantity $\Delta[X/Mg]_{med}$, the difference between a star's [X/Mg] and the median [X/Mg] of the plateau sample at a similar [Mg/H]. The median in [X/Mg] is calculated for the plateau sample in 0.1 dex wide bins centered at $[Mg/H] = -0.5, -0.4, -0.3, -0.2,$ and -0.1. The medians are shown by the solid black line in each panel in Figure 6. For a given star, $\Delta[X/Mg]_{med}$ is the difference between its measured [X/Mg] and the median [X/Mg] calculated for its [Mg/H] bin, thus removing overall trends with metallicity. $\Delta[X/Mg]_{med}$ is defined such that this quantity is positive if the star falls above the median. One can also calculate $\Delta[X/Mg]_{med}$ for a predicted abundance, such as from the two-process model. For clarity, we define $\Delta[X/Mg]_{med,obs}$ as $\Delta[X/Mg]_{med}$ calculated from the observed data, and $\Delta[X/Mg]_{med,2proc}$ as $\Delta[X/Mg]_{med}$ calculated from two-process predicted abundances.

We show an example of the expected trend in $\Delta[X/Mg]_{med}$ between different elements for the full plateau sample in Figure 7. The slope of the $\Delta[X/Mg]_{med}$ versus $\Delta[Fe/Mg]_{med}$ is noticeably steeper for Mn than for Si, consistent with with Mn having significantly more SN Ia contribution than Si. The slope differences echo that seen in Figure 5. We could examine such correlations in the median differences between all the element pairs in our sample, but there is an important caveat in this test: the effect of measurement uncertainty, which adds scatter and can induce spurious correlations because Mg affects both x- and y-axis quantities.

In the two-process model fit to only Fe and Mg, the ratio of process amplitudes A_{Ia}/A_{cc} is a simple linear transformation of linear {Fe/Mg} (Equation (8), Figure 5). Our six-element fit gives a less noisy estimate of A_{Ia}/A_{cc}, so it is preferable to
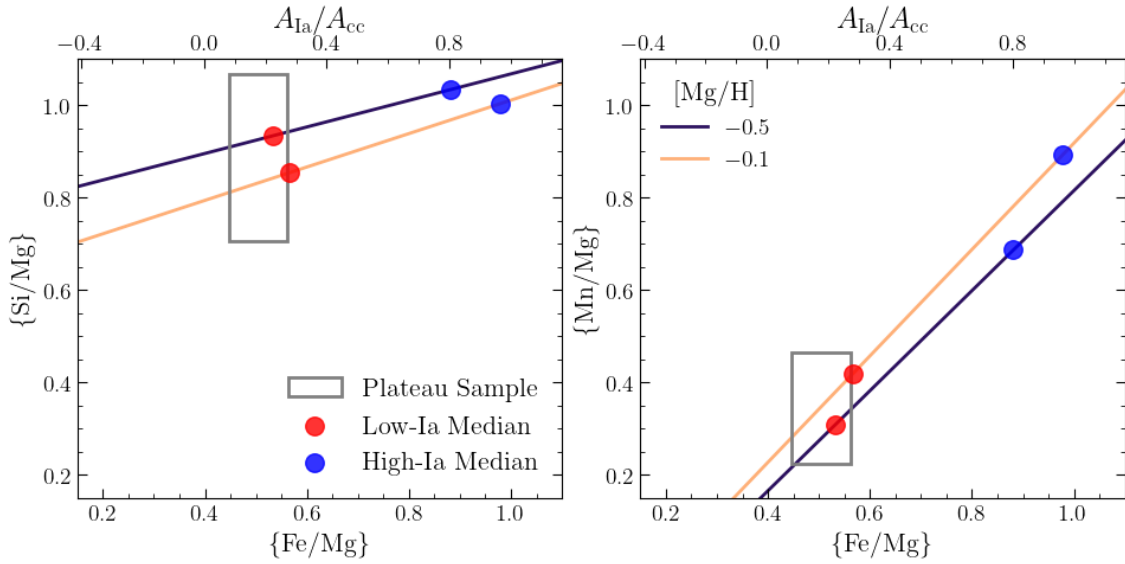
Figure 5. Linear abundances {Si/Mg} (left) and {Mn/Mg} (right) as a function of {Fe/Mg} (bottom axis) or, equivalently, A_{Ia}/A_{cc} (top axis, using Equation (8)) assuming $[Fe/Mg]_{cc} = -0.4$. Large red (blue) points indicate the median {X/Mg}–{Fe/Mg} value of the low-Ia (high-Ia) sequences calculated from the calibration sample at fixed [Mg/H]. The solid lines connect the median points to indicate the two-process predicted linear abundance values. The median points and connecting lines are calculated for $[Mg/H] = -0.5$ (dark purple line) and $[Mg/H] = -0.1$ (peach line). The gray box encloses the plateau sample: bounds are set by the sample selection in [Fe/Mg] converted to linear abundances and the 0.5–99.5 percentile range (99% of the data) in {X/Mg}.

$\Delta[Fe/Mg]_{med,obs}$ when examining the trends with other elements' $\Delta[X/Mg]_{med,obs}$. In a small fraction of stars, the six-element fit results in a best-fit A_{Ia}/A_{cc} that is outside the bounds of the A_{Ia}/A_{cc} calculated from the linear transformation of Fe/Mg (which is set by our sample selection), resulting in a more extended A_{Ia}/A_{cc} distribution compared to $\Delta[Fe/Mg]_{med,obs}$. An additional advantage of incorporating the two-process model is that we can use the predicted abundances to simulate how the elements should correlate if all intrinsic variation is explained by variation in SN Ia/CCSN ratio and the only noise is Gaussian with the reported uncertainties.

Figure 8 plots $\Delta[X/Mg]_{med}$ as a function of the SN Ia/CCSN ratio A_{Ia}/A_{cc}. For the observed data ($\Delta[X/Mg]_{med,obs}$, gray points in Figure 8), A_{Ia}/A_{cc} is calculated using the two-process model with the six-element fit assuming $[Fe/Mg]_{cc} = -0.4$. We compare this observed multielement abundance distribution to that predicted by the two-process model, where, by construction, the *only* source of intrinsic scatter is A_{Ia}/A_{cc}. To make this comparison, we generate a sample of predicted abundances by randomly sampling for each star from a Gaussian distribution centered on the two-process predicted [X/Mg] abundance (Equation (9)) with standard deviation equal to the reported APOGEE error. We then refit the star's A_{Ia} and A_{cc} with the perturbed abundances, so that the impact of noise on the two-process parameters is incorporated. Therefore, this sample reflects the predicted distribution of points if the only sources of scatter around the median are variations in A_{Ia}/A_{cc} and measurement error that is Gaussian with the reported uncertainty. The $\Delta[X/Mg]_{med,2proc}$ calculated from this [X/Mg] sampling procedure and the corresponding refitted A_{Ia}/A_{cc} are shown in Figure 8 by the light blue points.

The slope of the $\Delta[X/Mg]_{med}$ versus A_{Ia}/A_{cc} relation quantifies the SN Ia contribution to scatter on the low-Ia plateau. Slopes are calculated from a linear regression using inverse-variance weighting of the observational errors. The best-fit line calculated over all metallicities is shown in Figure 8 by

the solid lines corresponding to the colored points used for the regression. In Figure 9, we instead perform the linear regression in individual 0.1 dex [Mg/H] bins (the same as those used to calculate the medians and $\Delta[X/Mg]_{med}$) rather than over the entire plateau sample. The top panel of Figure 9 shows these slopes for all elements as a function of metallicity. For most elements, the slopes do not show notable metallicity dependence, so the trend seen for the full plateau sample in Figure 8 is representative. We note that for Si, the slope seen in Figure 7 appears significantly shallower in the observed slope in Figure 8, and Figure 9 has a $\Delta[Si/Mg]_{med,obs}$ versus A_{Ia}/A_{cc} slope of ≈ 0. This apparent slope change is partly due to the larger axis scale in Figure 8, but it arises primarily because some of the deviations are incorporated into A_{Ia}/A_{cc} from the fitting procedure. We would expect similar effects in the other fitting elements (O, Ca, Fe, and Ni).

In general, the Fe-peak elements such as Cr, Fe, Ni, V, and Mn, which are theoretically expected to have significant contribution from SN Ia, exhibit steeper $\Delta[X/Mg]_{med,obs}$ versus A_{Ia}/A_{cc} slopes. Conversely, elements with primarily CCSN contribution, such as the α elements O, Si, and Ca and the odd-Z elements Al and K, have observed slopes close to 0. The positive slopes in only elements with known significant SN Ia contribution imply that variation in the amount of SN Ia enrichment *is* a significant source of scatter on the low-Ia plateau. Therefore, the median trend through the low-Ia plateau does *not* represent "pure" CCSN enrichment, though the CCSN yield ratios could lie at the upper end of the observed scatter.

The slopes are similar between the observed data and two-process predictions for most elements, indicating that the two-process model predicts SN Ia contribution on the plateau well. The two elements with the largest differences between their observed and predicted slopes are Ce and C+N. The slope calculated with $\Delta[Ce/Mg]_{med,2proc}$ is steeper than the slope calculated with $\Delta[Ce/Mg]_{med,obs}$, indicating that the two-process model overpredicts the SN Ia contribution to Ce.
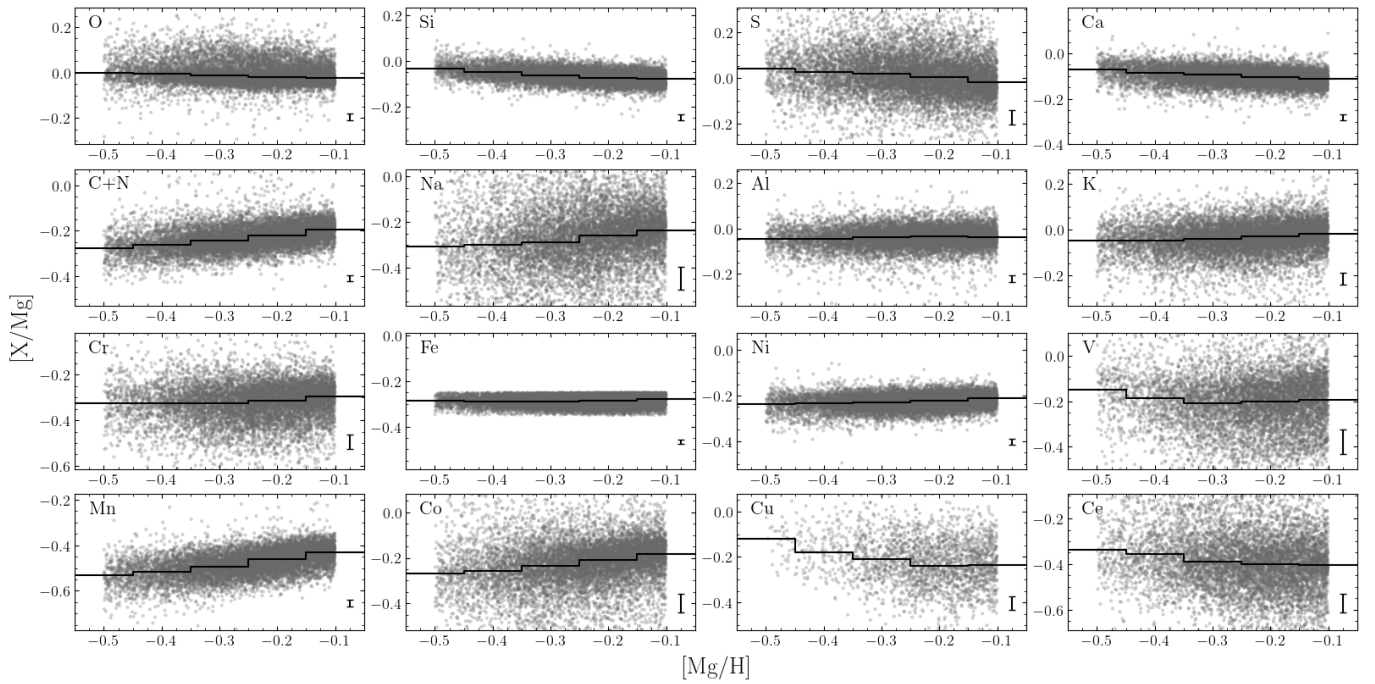
Figure 6. [X/Mg] vs. [Mg/H] for all stars in the plateau sample, for all elements considered in this study (except the reference element Mg). The scale of the *y*-axis in each panel is the same, shifted only by a zero-point to best accommodate the core of each element's distribution, so the level of scatter can be visually compared across all panels. The solid black line indicates the median value of [X/Mg], calculated in 0.1 dex wide [Mg/H] bins. The average observational uncertainty in [X/Mg] for each element, calculated by adding the [X/H] and [Mg/H] uncertainties in quadrature, are shown by the length of the error bars at the bottom right corner in each panel. Observed abundances for Na, Cr, V, Co, and Ce below an upper limit were removed following the procedure outlined in Appendix A.

Because the delayed contribution to Ce probably reflects AGB enrichment rather than SN Ia enrichment, it is not surprising that the linear trend inferred from the low-Ia and high-Ia medians does not apply within the low-Ia population (see Figure 5). Within our plateau sample, [Ce/Mg] exhibits little trend with A_{Ia}/A_{cc}, but large scatter. Conversely, the Δ[(C+N)/Mg]$_{med,2proc}$ slope is shallower than the Δ[(C+N)/Mg]$_{med,obs}$ slope. As with Ce, we expect the delayed contribution to C and N to come from AGB enrichment rather than SN Ia enrichment, so it is not surprising that the linear trend between the low-Ia and high-Ia medians does not describe the behavior within the low-Ia population. However, it is notable that the prediction is too steep for Ce but too shallow for C+N. This different behavior could possibly arise from different metallicity dependence of C, N, and Ce yields, but we have no full explanation for these trends. We suspect, but do not know, that most of the variation in [(C+N)/Mg] within our plateau sample comes from variation in birth [N/Mg], because CCSN are expected to be the primary sources of C while AGB stars make a large and metallicity-dependent contribution to N enrichment (see, e.g., B. H. Andrews et al. 2017; J. Rybizki et al. 2017; J. W. Johnson et al. 2023). The departures of C+N and Ce trends from those predicted based on the low-Ia and high-Ia median may provide clues to the physics of AGB enrichment in the early MW disk.

Other elements with small slope discrepancies include K, V, and Co, but these elements have large observational uncertainties, and non-Gaussian abundance errors or incorrect error estimates might affect the slopes. Finally, Ni also shows a small discrepancy between observed and predicted slopes. This is unexpected because Ni is considered a well-measured element in ASPCAP that we used in the six-element two-process fit and is not known to have any nucleosynthetic

contributions from processes outside of SN Ia and CCSN. When NLTE effects are accounted for, the ratio of Ni to Fe increases as metallicity decreases at subsolar metallicities (P. Eitner et al. 2023); this could possibly be a related signature. If the discrepancy is real, a possible explanation of the steeper Ni slope is that the population-averaged Ni yields are higher at plateau metallicities. A potential cause of different yields may be differences in the SN Ia progenitor landscape. Ni, Mn, and Cr yields are known to be different between sub-Chandrasekhar and near-Chandrasekhar mass SN Ia (C. Kobayashi et al. 2020b). Therefore, if the ratio of sub-Chandrasekhar to near-Chandrasekhar white dwarfs is different at the time of plateau formation compared to the current MW disk, this would result in different SN Ia yields on the plateau, even at the same metallicity. However, given that the Mn (and to a lesser extent, Cr) yields are also affected in this scenario, we would expect to also see a discrepant slope in Mn, but the difference between the Δ[Mn/Mg]$_{med,obs}$ and Δ[Mn/Mg]$_{med,2proc}$ slopes is smaller than for Ni.

4.2. Scatter Around the SN Ia/CCSN Correlation

While the slope quantifies the extent of A_{Ia}/A_{cc} variation on the plateau, the scatter around the linear fits is also interesting. We observe in Figure 8 that several elements have a more extended distribution in the data (gray points) than is predicted by the two-process model plus observational errors (blue points). This suggests that there may be an additional source of intrinsic variation in that element that is unrelated to the SN Ia/CCSN ratio, or that the reported measurement errors are underestimated.

We measure the scatter around the best-fit lines using the residual standard error (RSE, the standard deviation of residuals from the best-fit line). The bottom panel of
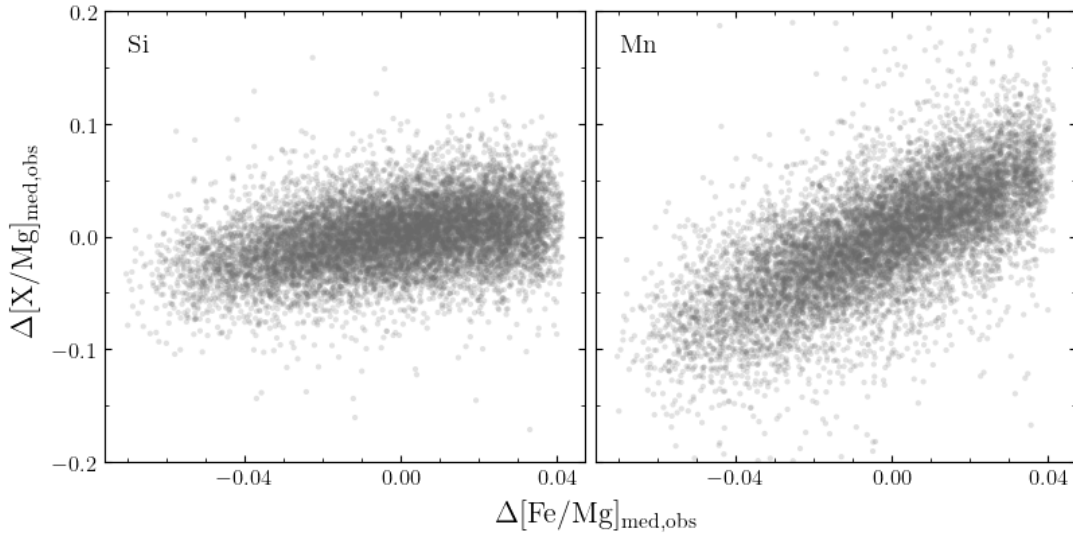
Figure 7. $\Delta[Si/Mg]_{med,obs}$ (left) and $\Delta[Mn/Mg]_{med,obs}$ (right) as a function of $\Delta[Fe/Mg]_{med,obs}$ for the plateau sample. Panels share the same y-axis scale. $\Delta[Mn/Mg]_{med,obs}$ shows the stronger correlation with $\Delta[Fe/Mg]_{med,obs}$ in this figure because both elements have substantial SN Ia contribution, while Si does not.

Figure 9 plots the RSE as a function of metallicity for all elements. Since the RSE is calculated from the best-fit line, it takes into account potential differences in the $\Delta[X/Mg]_{med}$ versus A_{Ia}/A_{cc} slopes between the observed data and two-process predictions. The measurement uncertainty is not explicitly included in the RSE calculation, though inverse-variance weighting is used for the linear regression to fit the line. Because the two-process prediction points incorporate observational scatter, a larger RSE for the data implies variation not explained by changes in the A_{Ia}/A_{cc} ratio plus Gaussian measurement uncertainties.

Broadly, most of the more well-measured elements (e.g., Si, Ca, Al, Fe, Ni, and Mn) show similar RSE between the data and prediction, indicating that measurement noise is sufficient to explain the remaining variation after contributions from a varying SN Ia/CCSN ratio are removed. In other words, the amount of SN Ia contribution and observational errors are the primary sources of variation on the plateau for these elements. Many of the elements that have larger observational uncertainties (e.g., S, Na, K, Cr, V, Co, Cu, and Ce) have higher observed RSE than predicted RSE. The explanation may be that the reported measurement uncertainties are still underestimated, or that the errors have non-Gaussian tails, since several of these elements (most notably S, Na, V, Cu, and Ce) have relatively weak lines that are often affected by blending. In these cases, the shallower spectral features make abundances difficult to measure and less reliable, particularly at lower abundances, which may increase the scatter. In some cases, especially Ce and perhaps C+N and Na, the larger observed RSE could reflect intrinsic scatter in an enrichment process that is neither CCSN nor SN Ia.

O is a fairly well-measured element with small observational uncertainties, but it has a slightly elevated observed RSE compared to its prediction. Looking at the corresponding panel of Figure 8, this may be explained by the upward splash of gray points toward lower A_{Ia}/A_{cc}, which is not well captured by the more symmetric scatter of the blue points. Although the reason is unclear, the $\Delta[O/Mg]_{med,obs}$ distribution is noticeably asymmetric: $\approx 7\%$ of the stars have $\Delta[O/Mg]_{med,obs} > 0.1$ while $\approx 1\%$ of stars have $\Delta[O/Mg]_{med,obs} < -0.1$ (recall that

$\Delta[X/Mg]_{med}$ is defined such that the distribution is centered at 0). Similarly, C+N has a small population of stars with higher $\Delta[(C+N)/Mg]_{med,obs}$ in Figure 8. We use the reported ASPCAP [C/Fe] measurement error as the total C+N uncertainty because C generally dominates over N by number (see W22 and S24), so C+N may also be affected by underestimated measurement uncertainty. Alternatively, the high $\Delta[(C+N)/Mg]_{med,obs}$ points could be a physical population affected by AGB mass transfer. Notably, while Ce has much larger observational errors than C+N, there is also a small population of stars with elevated $\Delta[Ce/Mg]_{med,obs}$. We have investigated these outlier populations and found that many of these stars are elevated in both $\Delta[(C+N)/Mg]_{med,obs}$ and $\Delta[Ce/Mg]_{med,obs}$, a likely signature of mass transfer, as found for the broader disk population by W22 (see their Figure 14).

For those elements where there is a metallicity trend, the RSE decreases with increasing [Mg/H]. For the predicted RSE, this is consistent with metal lines becoming stronger and easier to measure at higher metallicity, and thus the observational uncertainties decreasing. The most notable exception to this trend is Cu, which shows generally higher RSE at higher [Mg/H], but only $\approx 20\%$ of the stars in our sample have a Cu measurement at all, and there are fewer measurements in the low [Mg/H] bins.

The size of the difference, if any, between the observed and predicted RSE is also broadly the same across [Mg/H] bins. Ce is a significant exception to this because the difference between its observed and predicted RSE is largest at low [Mg/H]. The observational uncertainty could simply be more severely underestimated at lower metallicities. However, given that Ce is a primarily AGB element, there could be a more physical variation in the amount of AGB enrichment relative to SN Ia enrichment at lower metallicities. In such a scenario, different regions in the Galaxy may have different levels of AGB contribution at a fixed metallicity due to varying star formation histories and the time-dependence of the AGB yields. Since metal-poor stars are born from gas that experienced fewer enrichment events overall, they are more impacted by fluctuations in the level of AGB enrichment and the extent of gas mixing (or lack thereof) in their birth region.
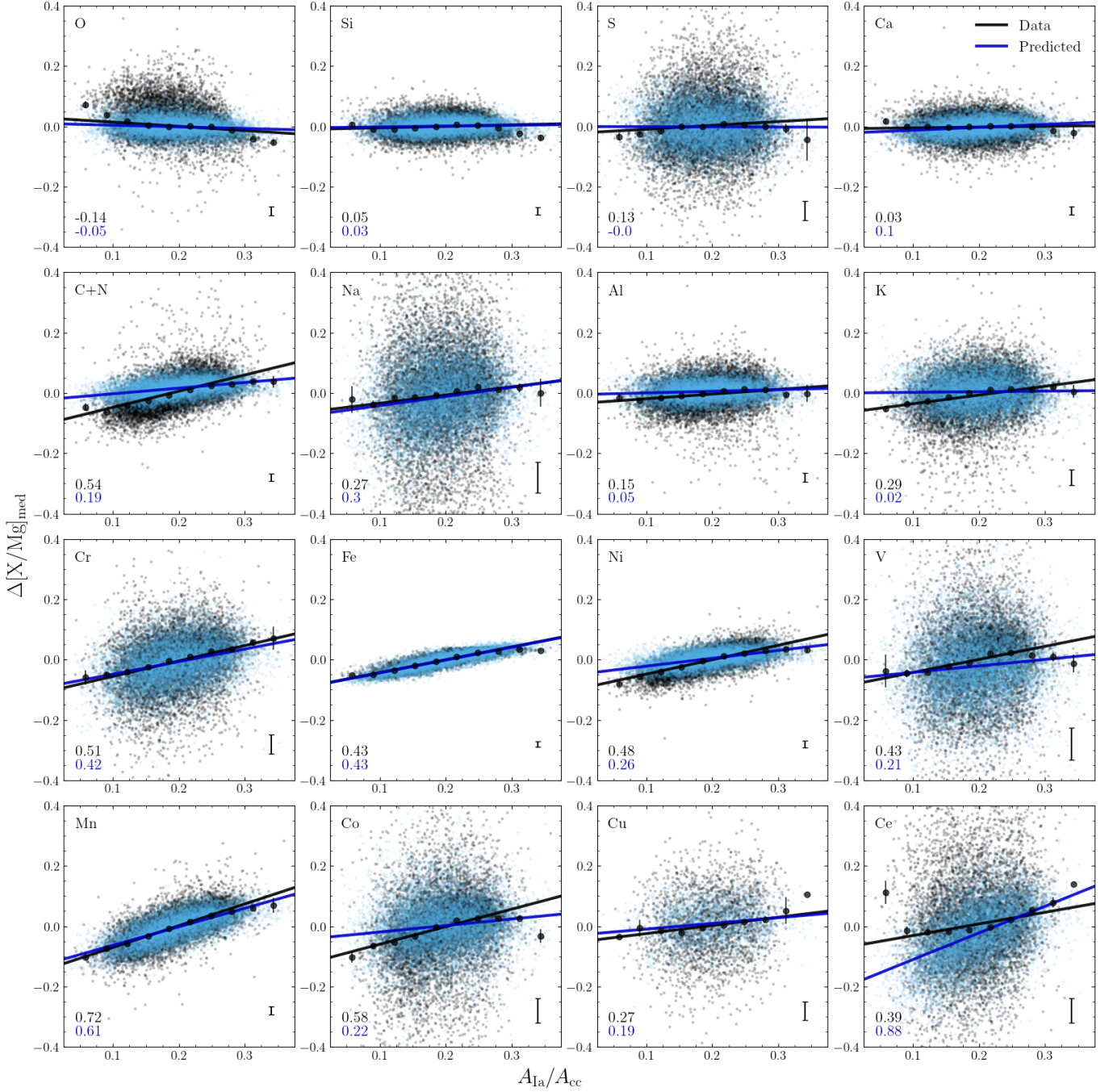
Figure 8. $\Delta[X/Mg]_{med}$ vs. A_{Ia}/A_{cc} for all elements except Mg, our reference element. Small black points are $\Delta[X/Mg]_{med,obs}$ values for individual stars (i.e., $\Delta[X/Mg]_{med}$ calculated from the observed [X/Mg] of each star), and A_{Ia}/A_{cc} is calculated from the six-element fit with assumed $[Fe/Mg]_{cc} = -0.4$. Large black points show the median of the black points in 10 evenly sized bins between the minimum and maximum A_{Ia}/A_{cc} values of the plateau sample, and their error bars indicate the uncertainty on each median from 1000 bootstrap resamplings. The thick black line shows the best-fit $\Delta[X/Mg]_{med,obs}$ vs. A_{Ia}/A_{cc} line and the slope value is reported by the black text in the bottom left of each panel. Small blue points show $\Delta[X/Mg]_{med,2proc}$ (i.e., $\Delta[X/Mg]_{med}$ calculated from the two-process prediction $[X/Mg]_{pred} = [X/H]_{pred} - [Mg/H]$, where $[X/H]_{pred}$ is given by Equation (2), resampled to account for reported observational error) for each star and new A_{Ia} and A_{cc} values derived from refitting to the new simulated $[X/H]_{pred}$. The thick blue line is the best-fit line between $\Delta[X/Mg]_{med,2proc}$ and refitted A_{Ia}/A_{cc}; the slope value is reported by the blue text in the bottom left of each panel. The length of the error bar on the bottom right of each panel represents the mean observational error for each element. Observed abundances for Na, Cr, V, Co, and Ce below an upper limit were removed following the procedure outlined in Appendix A.

4.3. Covariances between Elements

Correlations can be measured robustly even when observational uncertainties are comparable in magnitude to the intrinsic dispersion (Y.-S. Ting & D. H. Weinberg 2022). Furthermore, the residual correlation structure can encode information about additional enrichment pathways (beyond SN Ia and CCSN, which are accounted for by the two-process model), stochastic sampling of the interstellar medium (ISM), and potentially, interesting stellar evolution pathways such as binary mass transfer. We compute the covariance for each element pair ij as

$$c_{ij} = \langle(\Delta[X_i/Mg] - \langle\Delta[X_i/Mg]\rangle) \\ \times (\Delta[X_j/Mg] - \langle\Delta[X_j/Mg]\rangle)\rangle. \quad (10)$$
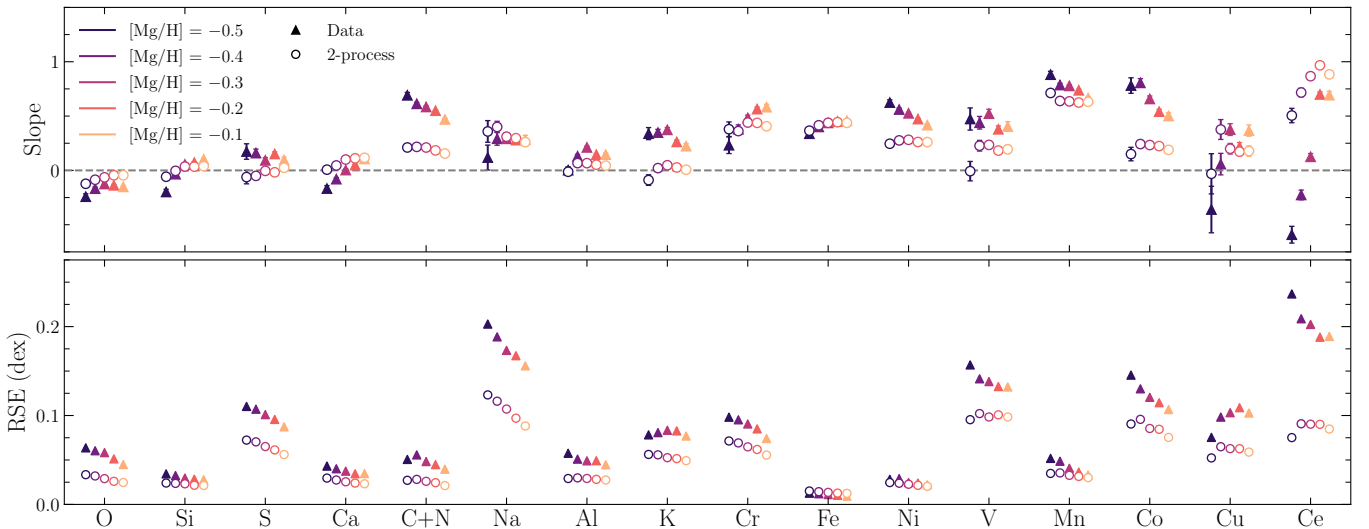
Figure 9. Slopes (top) and residual standard error (RSE, bottom) of the $\Delta[X/Mg]_{med}$ vs. A_{Ia}/A_{cc} plots as illustrated in Figure 8. The slope and RSE are calculated in 0.1 dex [Mg/H] bins centered at [Mg/H] = −0.1, −0.2, −0.3, −0.4, −0.5, to show the potential metallicity dependence of these quantities. Error bars in the top panel indicate the uncertainty on the slope from the linear regression covariance matrix; they are frequently smaller than the marker. The RSE in the bottom panel is calculated as the standard deviation of residuals from the linear fit. In both panels, filled triangles indicate the data (Figure 8, black lines) and the open circles indicate the two-process prediction with Gaussian observational errors (Figure 8, blue lines). Observed abundances for Na, Cr, V, Co, and Ce below an upper limit were removed prior to calculation of the slope and RSE following the procedure outlined in Appendix A.

Given that we are calculating the covariances of precomputed residuals, the expectation value in Equation (10), $\langle\Delta[X/Mg]\rangle$, is the mean of the residuals over the entire plateau sample which should be close to, but may not be exactly, 0. Furthermore, since the covariances are calculated for element pairs, the exclusion of any one element does not affect the presence of correlations (or lack thereof) between the remaining elements; similarly, the inclusion of a new element only adds the potential for correlations with that new element without affecting the others.

Figure 10 shows the covariance matrices for the observed residuals from the median, $\Delta[X/Mg]_{med,obs}$, in the left panel and the covariance of residuals from the two-process model, $\Delta[X/Mg]_{2proc}$, in the right panel. The size of each dot corresponds to the magnitude of the covariance, and the diagonals represent the variance of the residuals in each element. Blue filled dots represent positive covariances, while open red dots represent negative covariances.

The two-process model returns predictions in [X/H] (Equation (2)) such that the residual abundances (Equation (3)) are defined as $\Delta[X/H]_{2proc}$. To use Mg as the reference element, we use the following equation for the $\Delta[X/Mg]_{2proc}$ residuals:

$$\Delta[X/Mg]_{2proc} = ([X/H]_{meas} - [Mg/H]_{meas})$$
$$- ([X/H]_{2proc} - [Mg/H]_{2proc}) \quad (11)$$

$$= \Delta[X/H]_{2proc} - \Delta[Mg/H]_{2proc}. \quad (12)$$

$\Delta[X/H]_{2proc}$ is defined in Equation (3) and $\Delta[Mg/H]_{2proc}$ is defined in Equation (3) with X = Mg. As in W22, for the two-process residual covariance matrix (right panel), we subtract the covariance from measurement uncertainty, so that variation from *only* the two-process model remains. We also computed the covariance matrix of predicted median deviations, i.e., $\Delta[X/Mg]_{med,2proc}$ (blue points in Figure 8), but do not show it in Figure 10 because all values are positive (i.e., the two-

process model predicts that all residuals from the median should vary together to some extent).

The left panel of Figure 10 has many positive covariances, indicating that most elements tend to deviate from the median in the same direction. In particular, the Fe-peak elements, highlighted by the yellow square, have significant positive residuals; this is consistent with our previous result that variation in SN Ia/CCSN contribution is a significant source of correlated abundance scatter on the low-Ia plateau. The broadly positive residuals within an element group are also seen, though to a lesser extent, in the α elements highlighted by the purple box. We excluded the "Fe-cliff" element Cu from the Fe-peak yellow square here because it behaves differently from the other Fe-peak elements: Cu has (small) negative covariances with Cr and Co. Interestingly, C. Kobayashi et al. (2020a) find that Co and Cu are both largely produced by hypernovae, so one might expect these two elements in particular to be correlated.

The two-process model captures the variation in the SN Ia/CCSN ratio, so that the covariance in the two-process residuals should have the covariance from SN Ia/CCSN variation removed. The right panel of Figure 10 shows the covariance matrix of the two-process residuals. As expected, the signs of the two-process residual covariances are much more mixed, compared to the mostly positive median residual covariances. The magnitude of the covariances between Fe-peak elements have significantly decreased in the two-process residuals, and some have even changed sign, compared to the median residuals. However, V, Mn, and Co, which are odd-Z Fe-peak elements, still show some positive correlation with each other in the two-process residuals. The α elements already have small covariances, and their magnitudes are not significantly different between the median and two-process residuals. However, the Ca–O and Ca–Si covariances have different signs. Similarly, the light odd-Z elements like C+N, Na, and Al do not show any obvious correlations with each other in their two-process residuals, though some covariance signs change from the median residuals. The two-process residuals
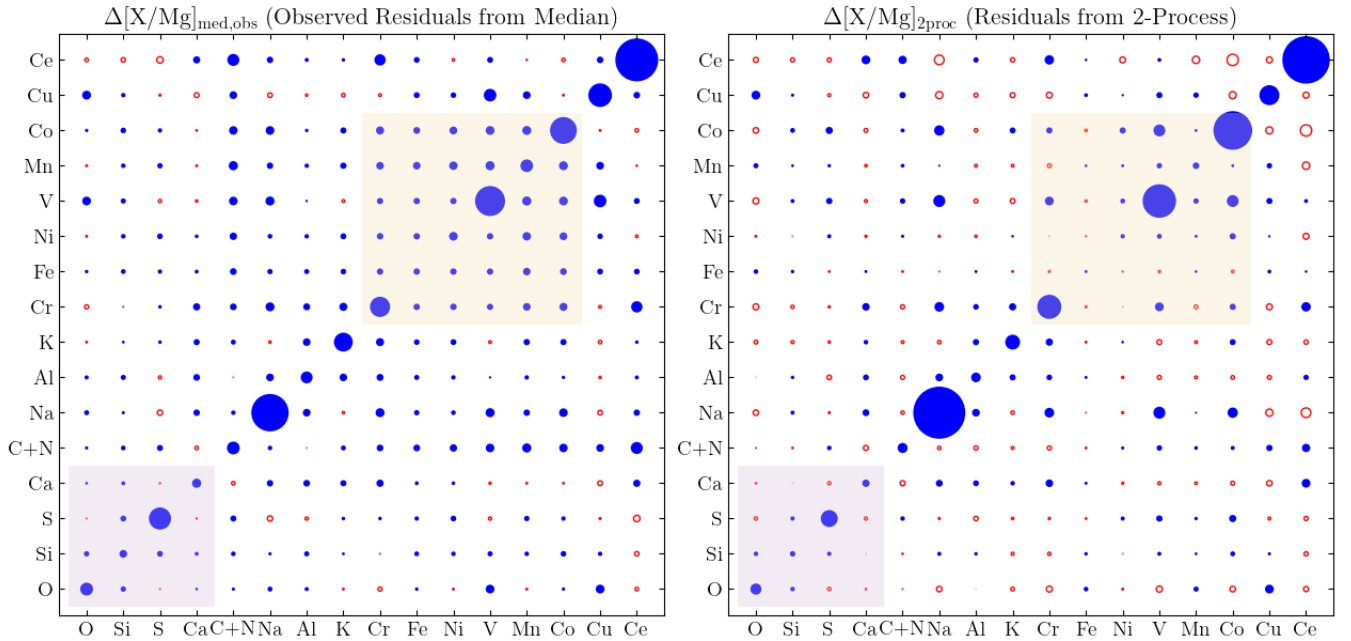
Figure 10. Covariance matrix of residuals $\Delta[X/Mg]$ for stars on the low-Ia plateau. In the left panel, $\Delta[X/Mg]$ are the observed residuals from the median plateau value, i.e., $\Delta[X/Mg]_{med,obs}$ as in Figure 8. In the right panel, $\Delta[X/Mg]$ are the two-process residual abundances as described in Equation (3), but with Mg used as the reference element (Equations (11)–(12)), and the covariance from measurement uncertainty has been subtracted. The α (Fe-peak) elements are highlighted by the purple (yellow) square in both panels. Blue filled circles and red open circles denote positive and negative values, respectively, with area proportional to the value of the covariance. Circles in both panels are on the same scale; for reference, in the left panel, the Na–Na circle is 0.03, O–O is 0.003, and Na–K is 0.000003.

of C+N are less correlated with those of the Fe-peak elements than the median residuals and are still positively correlated with Ce. Since C+N has contribution from a delayed process, this result indicates that this delayed process is not fully explained by the same delayed process (SN Ia) producing the Fe-peak elements; furthermore, since Ce is an AGB element, this suggests that an AGB process also contributes to C+N.

W22 removed outliers with a two-process residual greater than 10 times the measurement error for that element from their covariance calculations. If we also perform this cut, we find similar results to before, but the most affected element is Ce. More specifically, the Ce–(C+N) intrinsic $\Delta[X/Mg]_{2proc}$ covariance and Ce–Al $\Delta[X/Mg]_{med,obs}$ covariance change sign from positive to negative, while the Ce–Ni, Ce–Mn, and Ce–Co $\Delta[X/Mg]_{med,obs}$ covariances change from negative to positive. The rms scatter of Ce (diagonal element) also decreases. The majority of the removed outliers appear to be the same population of stars with strongly enhanced Ce and C+N found in W22, who propose that they are rare products of AGB mass transfer, where extra C+N and Ce from the AGB star are deposited onto the observed star's photosphere. Their presence here indicates that such mass transfer events occur in stars on the low-Ia plateau.

5. Discussion

In this work, we investigate the origin of multielement abundance scatter of stars in the low-Ia (high-α) plateau of the MW disk, with a particular focus on the effects of variation in the ratio of SN Ia to CCSN enrichment. Our test is based on the idea that elements with large SN Ia contribution should vary together, while the variation in elements with little SN Ia contribution should be smaller and less correlated. One could simply examine the correlations between deviations from the

median trends across many element pairs, but we use a two-process model to more precisely estimate the SN Ia/CCSN ratios and to predict what the plateau variations should look like if, indeed, the only sources of scatter are differences in SN Ia/CCSN ratio and measurement uncertainty.

First, we tested the effect of the assumed Fe-to-Mg ratio from pure-CCSN enrichment, $[Fe/Mg]_{cc}$, on the two-process model as formalized by W22. When the process amplitudes A_{Ia} and A_{cc} are inferred from only $[Mg/H]$ and $[Fe/Mg]$, the predicted linear $\{X/Mg\}$ abundance is simply a linear interpolation (or extrapolation) of the median $\{X/Mg\}$ ratios in the high- and low-Ia populations along $\{Fe/Mg\}$. It directly follows that the predicted abundances are independent of the assumed $[Fe/Mg]_{cc}$, and we show that this independence holds to an excellent approximation, even when using a multi-element χ^2 fit for A_{Ia} and A_{cc}.

Because of the linearity of the two-process model, the assumed pure-CCSN plateau value $[Fe/Mg]_{cc}$ only scales the process vectors and amplitudes, and it does so in a way that results in the same predicted abundances and without affecting the quality of the fit. This implies that the absolute scale of the q_{Ia} and q_{cc} process vectors, which can set empirical constraints on the IMF-averaged CCSN and SN Ia yields (e.g., E. J. Griffith et al. 2021), is poorly constrained. On the other hand, because the predicted abundances themselves do not change, we also demonstrate that residual abundance analyses —namely, the residual abundance trends in different populations (e.g., W22; S24; S. Hasselquist et al. 2024) and with Galactic position/kinematics (E. J. Griffith et al. 2025)—are robust to the $[Fe/Mg]_{cc}$ model assumption.

Next, we use the derived process amplitudes and predicted abundances from the two-process model to investigate elemental abundance scatter on the plateau. We examine $\Delta[X/Mg]_{med}$, the $[X/Mg]$ residuals from median trends in the

plateau, as a function of A_{Ia}/A_{cc}, the ratio of SN Ia/CCSN enrichment inferred from the two-process model. Our main result is that these values are positively correlated, especially in the Fe-peak elements, indicating that variation in the amount of SN Ia enrichment is a significant contributor to the [X/Mg] scatter on the low-Ia plateau. This interpretation is further supported by the Fe-peak elements having lower covariances in the two-process residuals than the median residuals.

Our results clearly establish that there is a systematic difference in the SN Ia/CCSN enrichment ratio between stars at the "top" of the low-Ia plateau and stars at the "bottom," a range of roughly 0.1 dex in [Mg/Fe]. This rules out the idea that the median [Mg/Fe] on the low-Ia plateau represents the core-collapse yield ratio [Mg/Fe]$_{cc}$, with abundance ratios scattering stochastically above and below because of, e.g., stochastic sampling of the CCSN population. It remains possible that [Mg/Fe]$_{cc}$ lies at the upper boundary of the plateau, at [Mg/Fe]$_{cc} = 0.35-0.4$ (see Figure 1). However, our results also lend credence to the idea that the true CCSN ratio is substantially higher, perhaps [Mg/Fe]$_{cc} \approx 0.6$, and the observed low-Ia plateau already includes substantial SN Ia enrichment (D. Maoz & O. Graur 2017; C. Conroy et al. 2022). Maintaining a nearly flat plateau at this intermediate [Mg/Fe] requires accelerating star formation if the ISM is well mixed (C. Conroy et al. 2022; B. Chen et al. 2023), though a similar effect may be achieved if early enrichment is spread throughout the circumgalactic medium and only slowly returns to the star-forming ISM (A. C. Mason et al. 2024).

For most elements we find good agreement between the predicted and observed slope of Δ[X/Mg]$_{med}$ versus A_{Ia}/A_{cc}, but there are exceptions. Most notably, the observed slope is steeper than predicted for C+N and shallower than predicted for Ce. For both abundances, we expect the delayed contribution comes from AGB stars rather than SN Ia, so disagreement with the two-process model is not too surprising, but we do not know why the sign of the discrepancy is different in these two cases. The intermediate mass stars that dominate AGB yields have lifetimes that are typically shorter than the ~1 Gyr median delay of the SN Ia enrichment, which can vary from 0.18 to 2.5 Gyr depending on the model (see Table 2 of L. O. Dubay et al. 2024).[6] The steeper trend of C+N is arguably the more natural result because of the larger change in C+N over the restricted time range of the thick disk compared to the interval between the thick and thin disks. Ni also has a slightly steeper observed than predicted trend, which suggests that the Ni/Fe yield ratio of SN Ia may be slightly higher in the low-Ia population.

The scatter about the Δ[X/Mg]$_{med}$ versus A_{Ia}/A_{cc} trend is higher for most elements than we predict based on the two-process model plus Gaussian scatter with the reported measurement error. In some cases, this excess scatter may indicate that the measurement uncertainties are underestimated, or at least that there are non-Gaussian tails to the error distribution. Recent studies have been mixed on how accurate the ASPCAP uncertainties are for DR17: J. Mead et al. (2024) found that the uncertainties are underestimated at dwarf galaxy metallicities, while A. Sinha et al. (2024) found that the uncertainties were sufficiently well-estimated in open clusters

near solar metallicity. The plateau sample analyzed in this work falls in between these two metallicity ranges. Future work on calibrating ASPCAP abundance uncertainties with high-resolution spectra will shed more light on this issue. Accurate abundance measurement uncertainties are essential for meaningful work on investigating the intrinsic abundance scatter of any population, not just the low-Ia plateau. Nonetheless, our main result that differences in the SN Ia/CCSN ratio are a significant cause of variation on the low-Ia plateau holds regardless of potential changes to the magnitude or distribution of measurement errors because it is based on the slope of the Δ[X/Mg]$_{med}$ versus A_{Ia}/A_{cc} trend, not the scatter around it.

Some of the excess scatter may be intrinsic. In particular, if AGB (or other delayed enrichment channels) make an important contribution to an element, then variation in the AGB/SN Ia ratio at a given SN Ia/CCSN ratio will lead to variation in that abundance (see E. J. Griffith et al. 2022 for Y and Ba in GALAH). Covariances of residual abundances can help to identify channels that affect multiple elements, but they become difficult to interpret when the scatter is only moderately larger than the measurement errors, which is typically the case for residual abundances in APOGEE.

Much of the attention in MW chemical evolution modeling has gone to understanding the difference in abundance trends between the thin and thick disks, and the bimodality of the [α/Fe] distribution at a given [Fe/H]. These features remain incompletely understood, with a variety of possible explanations. Extending earlier studies of the [α/Fe] scatter within the low-Ia population (S. Bertran de Lis et al. 2016; F. Vincenzo et al. 2021), our results show that there are significant variations of the SN Ia/CCSN ratio within the low-Ia population at fixed [Mg/H], producing coherent variations in the abundance ratios of many elements. However, the source of the variation itself is not obvious; potential causes may include stellar migration and/or uneven mixing of the ISM during the formation of the plateau. They further show distinctive behavior of some elements expected to have delayed contribution from AGB stars. Asteroseismic ages of APOGEE stars in the Kepler field show that the thick disk stars have a remarkably small age range, at least at the solar annulus (M. H. Pinsonneault et al. 2025). Producing the observed abundance variations within a short span of time is a challenge for models of the early evolution of the MW disk.

Acknowledgments

---

[6] L. O. Dubay et al. (2024) find that delay time distributions with fewer prompt SN Ia, which have median delay times of ~1−2.5 Gyr, result in multizone chemical evolution models that better fit the [α/Fe] distribution in the MW disk.

Appendix A
Upper Limits

Since ASPCAP does not naturally return upper limit estimates, we must turn to external analyses to determine the minimum possible abundance that can be measured in a given star. If the abundance measurement for a star falls below that limit, we assume that the spectral line was not strong enough for a detection and ASPCAP was likely fitting noise, and thus remove that measurement from analyses in Section 4. Figure 11 highlights the stars removed due to this upper limit analysis in red.

Because our sample is selected for high SNR like the BAWLAS catalog (C. R. Hayes et al. 2022), we prioritize the BAWLAS upper limit relations for the available overlapping elements. The BAWLAS upper limit relations are derived by synthesizing synthetic spectra over a grid of $T_{\rm eff}$ and element abundance, measuring where the line depths are some percent of the continuum value, and fitting a linear function of $T_{\rm eff}$ at fixed continuum threshold. We select the relations corresponding to a 1% continuum threshold. Then, for each star and each element, we calculate the upper limit of each line at that star's $T_{\rm eff}$, and then take the lowest line-by-line limit as the element's overall upper limit (so the line used can change with $T_{\rm eff}$). The elements most affected by this analysis are Na, V, and Ce, which all also showed an asymmetric scatter to [X/Mg] below the median. We find that $\approx$7% of the total Na measurements, $\approx$26% of the V measurements, and $\approx$10% of the total Ce measurements fall below upper limits; these fractions increase to $\gtrsim$75% for Na and $\gtrsim$90% for V and Ce of all measurements when we consider only stars where

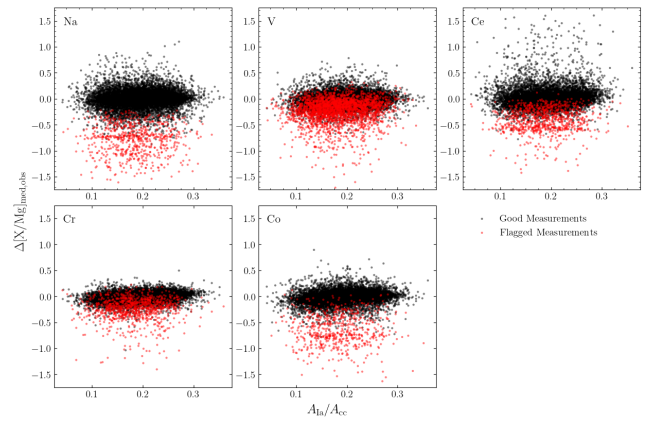**Figure 11.** $\Delta[{\rm X/Mg}]_{\rm med,obs}$ vs. $A_{\rm Ia}/A_{\rm cc}$, as in Figure 8, for elements significantly affected by upper limit removal (Na, V, Ce, Cr, and Co). Elements using the BAWLAS upper limit relations (C. R. Hayes et al. 2022) are in the top row while elements using the relations derived for dSph (M. Shetrone et al. 2025, in preparation) are in the bottom row. Measurements falling below the calculated upper limit for a given star's $T_{\rm eff}$ (Na, V, Ce) or $T_{\rm eff}$ and SNR (Cr, Co) and subsequently removed from analysis in Section 4 are highlighted in red. The remaining stars are plotted in black.

$\Delta[{\rm X/Mg}]_{\rm med,obs} < -0.4$ dex. While $\approx$18% of the total O measurements also fall below upper limits, the flagged measurements have approximately the same distribution as the unflagged measurements and their removal does not noticeably impact any analyses presented in Section 4, so we do not remove them.

For elements not included in the BAWLAS catalog, we use the upper limit relations from M. Shetrone et al. (2025, in preparation). Like BAWLAS, these relations were derived using a grid of synthetic spectra at a range of abundances and $T_{\rm eff}$. For each element, a weighted average of the line depth was measured for all individual lines; then, a function linear in $T_{\rm eff}$ and quadratic in $\log_{10}({\rm SNR})$ was fitted to the detection thresholds, defined where the average line depth is four times the noise per pixel. We note an important caveat in that these relations were derived for analysis of APOGEE dwarf spheroidal galaxies with lower metallicities and SNR than analyzed here; however, no other upper limits for APOGEE's spectra for non-BAWLAS elements are currently available. Using this set of upper limits, we find a significant impact on Cr and Co: $\approx$10% of the Cr measurements and $\approx$6% of the Co measurements fell below the detection threshold. Like Na, V, and Ce, Cr and Co also showed asymmetric scatter to low [X/Mg] prior to upper limit removal, and $\gtrsim$90% of Cr measurements and $\gtrsim$80% of Co measurements with $\Delta[{\rm X/Mg}]_{\rm med,obs} < -0.4$ dex were below upper limits. Additionally, there were seven flagged K measurements (0.06%), but we do not remove them from the Section 4 analysis.

Overall, removal of these upper limits results in a decrease in observed RSE of $\approx$0.1 dex for Na, $\approx$0.05 dex for V, $\approx$0.03 dex for Ce, $\approx$0.04 dex for Cr, and $\approx$0.09 dex for Co. For Na and Co, this RSE decrease exceeds the median observational error. The nature of the flagged measurements mostly having $\Delta[{\rm X/Mg}]_{\rm med,obs} \lesssim -0.4$ also generally results in the $\Delta[{\rm X/Mg}]_{\rm med,obs}$–$A_{\rm Ia}/A_{\rm cc}$ slopes decreasing (becoming flatter, since these five affected elements all have positive slopes).

Appendix B
Reproducibility

We have produced a public Git repository containing a Jupyter notebook that reproduces all of the figures in this paper. Also included with the repository are data tables for q values assuming different $[Fe/Mg]_{pl}$ (for reproducing Figure 2) and upper limits of the plateau sample in all elements (for reproducing Figure 11). The repository is accessible at https://github.com/tawnysit/plateau_variation.

ORCID iDs

Tawny Sit ⊙ https://orcid.org/0000-0001-8208-9755
David H. Weinberg ⊙ https://orcid.org/0000-0001-7775-7261
Emily J. Griffith ⊙ https://orcid.org/0000-0001-9345-9977

References

Abdurro'uf, Accetta, K., Aerts, C., et al. 2022, ApJS, 259, 35
Adibekyan, V. Z., Sousa, S. G., Santos, N. C., et al. 2012, A&A, 545, A32
Andrews, B. H., Weinberg, D. H., Schönrich, R., & Johnson, J. A. 2017, ApJ, 835, 224
Astropy Collaboration, Price-Whelan, A. M., Lim, P. L., et al. 2022, ApJ, 935, 167
Astropy Collaboration, Price-Whelan, A. M., Sipőcz, B. M., et al. 2018, AJ, 156, 123
Astropy Collaboration, Robitaille, T. P., Tollerud, E. J., et al. 2013, A&A, 558, A33
Bensby, T., Feltzing, S., & Lundström, I. 2003, A&A, 410, 527
Bertran de Lis, S., Allende Prieto, C., Majewski, S. R., et al. 2016, A&A, 590, A74
Chen, B., Hayden, M. R., Sharma, S., et al. 2023, MNRAS, 523, 3791
Conroy, C., Weinberg, D. H., Naidu, R. P., et al. 2022, arXiv:2204.02989
Dubay, L. O., Johnson, J. A., & Johnson, J. W. 2024, ApJ, 973, 55
Eitner, P., Bergemann, M., Ruiter, A. J., et al. 2023, A&A, 677, A151
Feltzing, S., Bensby, T., & Lundström, I. 2003, A&A, 397, L1
Fuhrmann, K. 1998, A&A, 338, 161
Griffith, E., Johnson, J. A., & Weinberg, D. H. 2019, ApJ, 886, 84
Griffith, E., Weinberg, D. H., Johnson, J. A., et al. 2021, ApJ, 909, 77
Griffith, E. J., Hogg, D. W., Dalcanton, J. J., et al. 2024, AJ, 167, 98
Griffith, E. J., Hogg, D. W., Hasselquist, S., et al. 2025, AJ, 169, 280
Griffith, E. J., Sukhbold, T., Weinberg, D. H., et al. 2021, ApJ, 921, 73
Griffith, E. J., Weinberg, D. H., Buder, S., et al. 2022, ApJ, 931, 23
Harris, C. R., Millman, K. J., van der Walt, S. J., et al. 2020, Natur, 585, 357
Hasselquist, S., Hayes, C. R., Griffith, E. J., et al. 2024, ApJ, 974, 227
Hayden, M. R., Recio-Blanco, A., de Laverny, P., Mikolaitis, S., & Worley, C. C. 2017, A&A, 608, L1
Hayes, C. R., Masseron, T., Sobeck, J., et al. 2022, ApJS, 262, 34
Hunter, J. D. 2007, CSE, 9, 90
Johnson, J. W., Weinberg, D. H., Vincenzo, F., Bird, J. C., & Griffith, E. J. 2023, MNRAS, 520, 782
Jönsson, H., Holtzman, J. A., Allende Prieto, C., et al. 2020, AJ, 160, 120
Kobayashi, C., Karakas, A. I., & Lugaro, M. 2020a, ApJ, 900, 179
Kobayashi, C., Leung, S.-C., & Nomoto, K. 2020b, ApJ, 895, 138
Leung, H. W., & Bovy, J. 2019, MNRAS, 489, 2079
Mackereth, J. T., & Bovy, J. 2018, PASP, 130, 114501
Majewski, S. R., Schiavon, R. P., Frinchaboy, P. M., et al. 2017, AJ, 154, 94
Maoz, D., & Graur, O. 2017, ApJ, 848, 25
Mason, A. C., Crain, R. A., Schiavon, R. P., et al. 2024, MNRAS, 533, 184
Matteucci, F., & Greggio, L. 1986, A&A, 154, 279
McKinney, W. 2010, in Proc. 9th Python in Science Conf., ed. S. van der Walt & J. Millman (Austin, TX: SciPy), 56
McWilliam, A. 1997, ARA&A, 35, 503
Mead, J., Ness, M., Andersson, E., Griffith, E. J., & Horta, D. 2024, ApJ, 974, 186
Ness, M. K., Johnston, K. V., Blancato, K., et al. 2019, ApJ, 883, 177
Ness, M. K., Wheeler, A. J., McKinnon, K., et al. 2022, ApJ, 926, 144
Nomoto, K., Kobayashi, C., & Tominaga, N. 2013, ARA&A, 51, 457
The pandas development team 2023, pandas-dev/pandas: Pandas, v2.0.3, Zenodo, doi:10.5281/zenodo.3509134
Pinsonneault, M. H., Zinn, J. C., Tayar, J., et al. 2025, ApJS, 276, 69
Ratcliffe, B. L., & Ness, M. K. 2023, ApJ, 943, 92
Romano, D., & Matteucci, F. 2007, MNRAS, 378, L59
Rybizki, J., Just, A., & Rix, H.-W. 2017, A&A, 605, A59
Sinha, A., Zasowski, G., Frinchaboy, P., et al. 2024, ApJ, 975, 89
Sit, T., Weinberg, D. H., Wheeler, A., et al. 2024, ApJ, 970, 180
Ting, Y.-S., & Weinberg, D. H. 2022, ApJ, 927, 209
Vincenzo, F., Weinberg, D. H., Miglio, A., Lane, R. R., & Roman-Lopes, A. 2021, MNRAS, 508, 5903
Virtanen, P., Gommers, R., Oliphant, T. E., et al. 2020, NatMe, 17, 261
Weinberg, D. H., Holtzman, J. A., Hasselquist, S., et al. 2019, ApJ, 874, 102
Weinberg, D. H., Holtzman, J. A., Johnson, J. A., et al. 2022, ApJS, 260, 32
Woosley, S. E., & Weaver, T. A. 1995, ApJS, 101, 181